PAPER

View Article Online
View Journal | View Issue

Raman and NMR spectroscopic and theoretical investigations of the cubic laves-phases REAl₂ (RE = Sc, Y, La, Yb, Lu)†

Elias C. J. Gießelmann, [a] Stefan Engel, [a] Weronika Kostusiak,[b,c] Yuemei Zhang, [b] Petra Herbeck-Engel,[d] Guido Kickelbick [a] and Oliver Janka *[a]

The cubic Laves-phase aluminides REAl₂ with RE = Sc, Y, La, Yb and Lu were prepared from the elements by arc-melting or using refractory metal ampoules and induction heating. They all crystallize in the cubic crystal system with space group $Fd\bar{3}m$ and adopt the MgCu₂ type structure. The title compounds were characterized by powder X-ray diffraction and spectroscopically investigated using Raman and ^{27}Al and in the case of ScAl₂ by ^{45}Sc solid-state MAS NMR. In both, the Raman and NMR spectra, the aluminides exhibit only one signal due to the crystal structure. DFT calculations were used to calculate Bader charges illustrating the charge transfer in these compounds along with NMR parameters and densities of states. Finally, the bonding situation was assessed by means of ELF calculations rendering these compounds aluminides with positively charged RE$^{\delta+}$ cations embedded in an [Al₂]$^{\delta-}$ polyanion.

1 Introduction

Intermetallic aluminium compounds are an interesting class of materials, since they play a major role in the formation of high-strength aluminium alloys formed during precipitation hardening.[1,2] In Mg–Cu–Al alloys for example, the so-called *S*-phase (MgCuAl₂, *Cmcm*) forms during annealing.[3–5] When searching the Pearson database,[6] it becomes evident that Al forms binary compounds with almost every other element in the periodic table. Exceptions are the alkali-metals Na and heavier (Li compounds do exist), Cd and Hg, In and Tl as well as Pm and most of the actinides. The latter ones, however, are probably unknown due to a lack of accessibility. Amongst these, the alkaline-earth, group 3 and rare-earth metals and some of the actinides form compounds with the general formula MAl₂ (Ca–Ba, Sc, Y, La–Nd, Sm–Lu, Th, U–Pu[7–13]) which adopt the cubic Laves-phase structure type MgCu₂ ($Fd\bar{3}m$). Having numerous isostructural compounds at hand enables the investigation of *e.g.* physical properties like their

wear- and corrosion-resistance, their magnetic or superconductive, their low-temperature behaviour or their hydrogen storage capabilities also in dependence of the constituent elements.[14–17] When drawing back to the MAl₂ compounds, the compounds differ with respect to their unit cell parameter, but both crystallographic sites are special positions (M on 8*b* (3/8, 3/8, 3/8); Al on 16*c* (0,0,0)). Therefore, the sizes of the respective M atoms at least partially influence the lattice parameters. However, the elements differ significantly with respect to their electronegativities, and their valence electron configuration. In all cases, the Al atoms are more electronegative than the M atoms rendering these compounds aluminides. While the alkaline-earth atoms can supply a maximum of two electrons, elements of group 3 and the rare-earth atoms can supply up to three electrons. Exception of this rule are Eu and Yb, which are two electron metals in their elemental form.[18,19] This in turn leads to differences in the respective negative charges on the Al atoms in the binary MAl₂ compounds.

Solid-state Nuclear Magnetic Resonance (NMR) spectroscopy is a strong, site specific method for the characterization of compounds containing NMR active nuclei and known and used for several decades. Having 100% natural abundance the ^{27}Al nucleus ($I = 5/2$) is an excellent candidate for NMR spectroscopic experiments, however, a medium-sized nuclear electric quadrupole moment ($e_Q = 0.15 \times 10^{-28}$ m²) and a moderately high gyromagnetic ratio ($\gamma = 6.976 \times 10^7$ rad T^{-1} s^{-1}) can complicate the interpretation of its spectra.[20,21] Still, ^{27}Al (MAS-)NMR is nowadays a widely established technique for structural characterization in different material classes.[22–26]

[a] Inorganic Solid-State Chemistry, Saarland University, Campus C4.1, 66123 Saarbrücken, Germany. E-mail: oliver.janka@uni-saarland.de
[b] Department of Chemistry and Physics, Warren Wilson College, Swannanoa, NC, 28778, USA
[c] Department of Chemistry, University of Wroclaw, F. Joliot-Curie 14, 50-383 Wroclaw, Poland
[d] INM Leibniz Institute for New Materials, Campus D2.2, 66123 Saarbrücken, Germany

†Electronic supplementary information (ESI) available: Additional powder X-ray data, individual ^{27}Al NMR spectra. See DOI: https://doi.org/10.1039/d3dt00141e

Especially in the last twenty years it has been established as a versatile method for additional characterization of intermetallic compounds.[27] And although this class of compounds has metallic character, the method can be used to gain a plethora of information such as validation of crystallographic structures, local environments, solid solutions and more. And although many ternary compounds have been characterized by NMR (*e.g.* the equiatomic ScTAl compounds,[28] the ScT$_2$Al Heusler phases,[29] the gold compounds Na$_2$Au$_3$Al,[30] AEAuX,[31] AEAu$_2$Al$_2$,[32] or the platinides Ba$_3$Pt$_4$Al$_4$[33] or Sr$_2$Pt$_3$Al$_8$[34]) there is a significant lack of comparing studies about a larger group of isostructural compounds. As examples for the latter, the MTAl$_2$[35,36] or the RE$_{10}$TAl$_3$ series[37] should be mentioned.

Here, a combining study on the rare-earth aluminides REAl$_2$ for the elements Sc, Y, La, Yb and Lu is presented. These aluminides are Pauli-paramagnetic (no localized magnetic moments, only conduction electrons) and exhibit only one crystallographic Al site, rendering them ideal candidates for systematic ^{27}Al NMR studies. Individual studies on some of the compounds have already been reported before,[38–41] however, a comparing work of the ^{27}Al NMR data is missing and ScAl$_2$ has not been characterized before. For this compound, in addition to ^{27}Al also ^{45}Sc NMR data could be obtained. Raman spectroscopic investigations were conducted on all prepared samples, which help to understand these compounds even further. Additionally, quantum-chemical calculations were carried out to help with the interpretation of the NMR data and to calculate Bader charges which can be used to analyse the anionic character of the $[Al_2]^{\delta-}$ network. The bonding situation was assessed using the electron localization function ELF.

2 Experimental

2.1 Synthesis

Aluminium pellets (99.99%, Onyxmet), scandium (99.98%; Onyxmet), yttrium (99.99%; Onyxmet), lanthanum (99.95%, Onyxmet), ytterbium (99.95%, Onyxmet) and lutetium (99.95%; Onyxmet) chunks were used for the reported syntheses. Lanthanum pieces were stored under an argon atmosphere, surface contaminations on the pieces were removed mechanically in an argon filled glovebox. The elements were weighed in the ideal stochiometric ratio of RE : Al = 1 : 2 and subsequently arc-melted in water-cooled copper crucibles in an argon atmosphere of about 800 mbar.[42] The argon gas was purified over a titanium sponge (873 K), molecular sieve and silica gel prior to the use. The obtained buttons were remelted four to five times to improve the homogeneity. Powdered as-cast LuAl$_2$ was loaded into a corundum crucible which was sealed in an evacuated silica tube and annealed at 1073 K for 48 h followed by cooling to RT within 48 h. The other samples were used without any further heat treatment. The ytterbium compound was synthesized in an arc-welded niobium ampoule[43] due to the low boiling point of ytterbium metal (1496 K[18]). The Nb ampoule was heated for 2 h to approximately 1200 K in an induction furnace (Trumpf Hüttinger,

Truheat HF 5010) under argon atmosphere. All samples show metallic lustre, ground powders are grey and stable in air over months.

2.2 X-ray diffraction

Powder X-ray diffraction (PXRD) patterns of the pulverized samples were recorded at room temperature on a D8-A25-Advance diffractometer (Bruker, Karlsruhe, Germany) in Bragg Brentano θ-θ-geometry (goniometer radius 280 mm) with Cu K$_\alpha$-radiation (λ = 154.0596 pm). A 12 µm Ni foil working as K$_\beta$ filter and a variable divergence slit were mounted at the primary beam side. A LYNXEYE detector with 192 channels was used at the secondary beam side. Experiments were carried out in a 2θ range of 6–130° with a step size of 0.013° and a total scan time of 1 h. The recorded data was evaluated using the Bruker TOPAS 5.0 software.[44]

2.3 Solid-state NMR

^{27}Al and ^{45}Sc solid-state NMR spectra were recorded using a Bruker Avance III 400 WB spectrometer at 104.31 and 97.24 MHz using magic-angle spinning (MAS) conditions. The samples were used as fine powders. To reduce density and electrical conductivity, samples were mixed with dried sodium chloride in a 1 : 9 ratio. The diluted samples were loaded into a cylindrical ZrO$_2$ rotor with a diameter of 4 mm and spun at the magic angle with 13 kHz. All experiments conducted were single-pulse with a typical pulse length of 0.83 µs and a relaxation delay of 1 s. Resonance shifts were referenced to 1 molar AlCl$_3$ and ScCl$_3$ solutions in H$_2$O. The NMR spectra were recorded using the Bruker Topspin software,[45] the analysis was performed with the help of the DMFit software.[46]

2.4 Raman measurements

For the acquisition of the Raman spectra, a Raman microscope LabRAM HR Evolution HORIBA Jobin Yvon A (Longmujeau, France) equipped with 532 and 633 nm Lasers (Melles Griot, IDEX Optics and Photonics, Albuquerque, USA) and an 1800 lines mm^{-1} grating and a 100er LWD objective was used.

2.5 Theoretical calculations

Density functional theory (DFT) calculations of the REAl$_2$ series (RE = Sc, Y, La, Yb, Lu) were performed using the projector augmented wave method (PAW) of Blöchl[47,48] coded in the Vienna *ab initio* simulation package (VASP).[49,50] All VASP calculations employed the generalized gradient approximation (GGA) with exchange and correlation treated by Perdew–Burke–Enzerhof (PBE).[51] The cut-off energy for the plane wave calculations was set to 500 eV and the Brillouin zone integration was carried out using 9 × 9 × 9 k-point meshes. NMR parameters were evaluated through the field gradient tensor calculations in VASP with the nuclear quadrupole moment of 146.6 mb for ^{27}Al and −220 mb for ^{45}Sc. The Bader charge analysis was based on VASP calculations with subsequent calculations using the Bader program developed by the Henkelman group.[52–54] Chemical bonding was explored *via* Electron

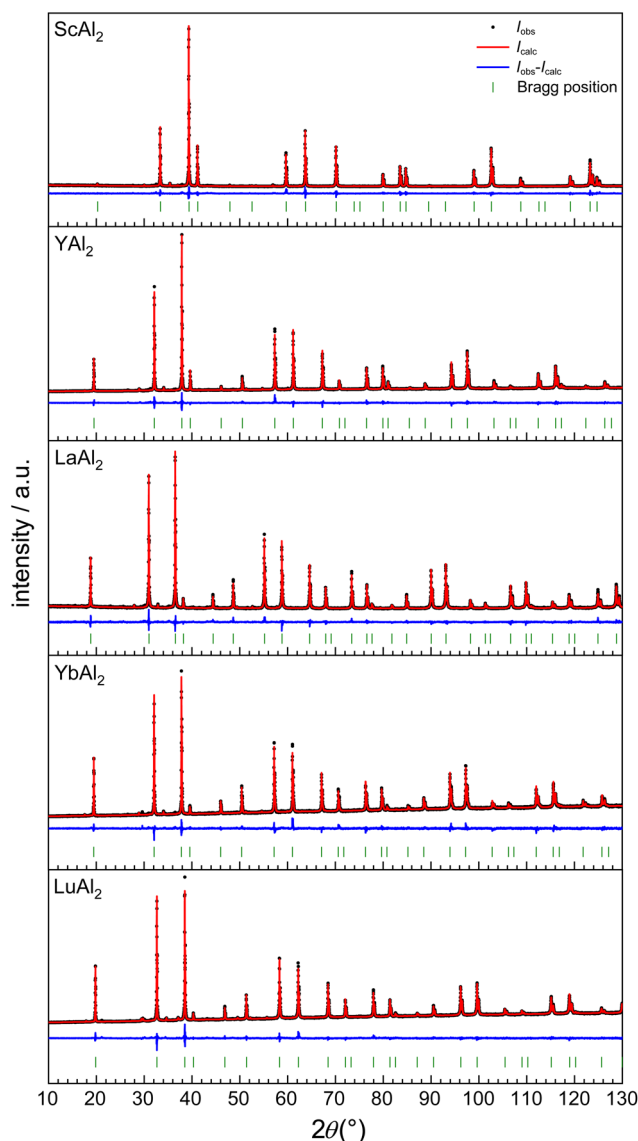Localization Functions (ELF)[55,56] obtained from the VASP calculations.

3 Results and discussion

3.1 Synthesis & X-ray diffraction

Phase pure samples, according to powder X-ray diffraction experiments, for all five rare-earth elements were obtained as described above. The diffraction patterns are shown in Fig. 1. The lattice parameters for the cubic compounds prepared in this work and from the literature are summarized in Table 1. As expected, the lattice parameters decrease with decreasing ionic radius[57,58] of the rare-earth atoms and show an almost

Table 1 Lattice parameters, determined by Rietveld analysis from the recorded PXRD patterns of the cubic Laves-phases (MgCu$_2$ type, $Fd\bar{3}m$) and from the literature
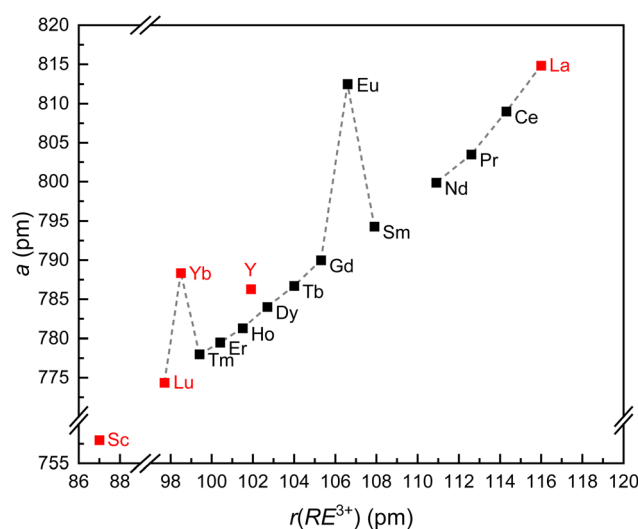
Compound	a/pm	Ref.
ScAl$_2$	757.98(1)	This work
ScAl$_2$	758.0	62
YAl$_2$	786.29(1)	This work
YAl$_2$	786.0	12
LaAl$_2$	814.85(1)	This work
LaAl$_2$	816.9	63
CeAl$_2$	809.0	63
PrAl$_2$	803.5	11
NdAl$_2$	799.9	11
SmAl$_2$	794.3	11
EuAl$_2$	812.5	64
GdAl$_2$	790.0	13
TbAl$_2$	786.7	13
DyAl$_2$	784.0	13
HoAl$_2$	781.3	13
ErAl$_2$	779.5	13
TmAl$_2$	778.0	64
YbAl$_2$	788.36(1)	This work
YbAl$_2$	787.7	64
LuAl$_2$	774.37(1)	This work
LuAl$_2$ – annealed	774.24(1)	This work
LuAl$_2$	774.2	64

linear trend as it is expected due to the lanthanide contraction (Fig. 2). Exceptions from this trend are observed for EuAl$_2$ and YbAl$_2$. While the Eu atoms in EuAl$_2$ exhibit a stable divalent state,[59] YbAl$_2$ was shown to be intermediate valent with a valence close to +2.4 at 300 K.[60,61] Since both Eu^{2+} and Yb^{2+} are significantly larger compared to their trivalent counterparts (r(Eu^{2+}) = 125 pm $vs.$ r(Eu^{3+}) = 107 pm and r(Yb^{2+}) = 114 pm $vs.$ r(Yb^{3+}) = 99 pm; all given for CN = 8 [57,58]), signficantly enlarged unit cells are observed for these two compounds.

A more detailed analysis of the diffraction patterns indicates that all samples contain a certain degree of strain since

Fig. 1 Powder X-ray diffraction pattern of the REAl$_2$ compounds (RE = Sc, Y, La, Yb and Lu; top to bottom) crystallizing in the cubic MgCu$_2$ type structure ($Fd\bar{3}m$). The experimental data is shown as black dots, the fit as red line and the difference in blue. The green ticks indicate the Bragg positions.

Fig. 2 Lattice parameters of the REAl$_2$ compounds (RE = Sc, Y, La–Nd, Sm–Lu) crystallizing in the cubic MgCu$_2$ type structure ($Fd\bar{3}m$) plotted $versus$ their respective ionic radius for CN = 8.

they were used without annealing. The largest strain is observed for the samples of YAl_2 and $LuAl_2$, while $ScAl_2$ for example shows almost no strain. The work of Yuan and coworkers reported,[38] that a thermal treatment of the $LuAl_2$ sample improves the quality of the NMR spectrum with respect to the line broadening and assymmetry of the central transition line shape, however, the resonance frequency and the quadrupolar coupling are not affected. This might indicate that their initial sample also contained certain amounts of strain. Subsequently, the as-cast $LuAl_2$ sample from this work was annealed for 48 h at 1073 K, which led to a significant decrease of the strain.

3.2 Crystal chemistry

The $REAl_2$ members (RE = Sc, Y, La, Yb, Lu) all crystallize in the cubic crystal system with space group $Fd\bar{3}m$ and adopt the so-called cubic Laves-phase ($MgCu_2$ type). The structure contains one RE and one Al site, with the Al atoms forming empty Al_4 tetrahedra that are connected to other tetrahedra *via* all atoms forming a network (Fig. 3, left). The RE atoms reside in the cavities of this framework. When looking at the arrangement of the RE atoms, an arrangement similar to cubic diamond can be observed. In the following paragraph, the structure will be briefly discussed using $ScAl_2$ as example. The Al atoms are surrounded by six Al and six Sc atoms in the shape of a compressed icosahedron (Fig. 3, right). The Al atoms form two opposing triangular faces while the six Sc atoms are located near the equatorial plane, forming an undulating six-membered ring. The Sc atoms exhibit a coordination number of 16 arranged as Frank-Kasper polyhedron ($Sc@Sc_4Al_{12}$; Fig. 3, middle). Due to the high site symmetries (Sc: $8b$, $\bar{4}3m$; Al: $16c$, $.3m$) and the symmetric coordination environment, one can derive that the asymmetry parameters η_Q for all ^{27}Al and the ^{45}Sc NMR spectra should be zero. At the same time, the nuclei of both Sc and Al exhibit a quadrupole moment. Therefore, the quadrupolar interaction of both nuclei is expected to be observed in their respective NMR spectra.

3.3 Solid State NMR spectroscopy

All five ^{27}Al MAS spectra recorded with single-pulse excitation experiments are shown in Fig. 4 (left). As described in the previous section, one resonance originating from one crystallographically independent Al site in the crystal structure is expected. All spectra show one sharp central line, originating from the $|+1/2\rangle \leftrightarrow |-1/2\rangle$ transition. All of them also show a wide spinning side band manifold caused by the $|\pm1/2\rangle \leftrightarrow |\pm3/2\rangle$ and $|\pm3/2\rangle \leftrightarrow |\pm5/2\rangle$ transitions, which are observable due to quadrupolar interactions. All resonance lines are significantly shifted compared to an aqueous solution of Al^{3+} within a range of 200 up to 950 ppm. This is caused by the interaction of the magnetic moment of the active ^{27}Al nuclei, the same is true for ^{45}Sc, with the conduction electrons of the metallic material. This is known as the Knight shift. To analyse the spectra, in a first step all central transitions were fitted with simple Gaussian-Lorentz lines. As can be seen on the right part of Fig. 4, all line shapes can be described with a Gaussian-Lorentz fit in a satisfying fashion. However, in the spectra of YAl_2, $LuAl_2$ and $YbAl_2$ the central transition shows a broad half-width and anisotropy with a shoulder on the left side.

Table 2 summarizes the relevant experimentally determined NMR parameters along with the ones from the DFT calculations. For some cases (RE = Y, La) the spectra could be simulated quite well using the values from DFT calculations. In these cases, the C_Q parameters were not refined. Due to the cubic symmetry of the structure, the asymmetry parameter η_Q must be zero, which agrees with the result of the DFT calculations. From the resonance shifts δ gained by fitting the data, the Knight shift contribution δ_K can be calculated using the NMR parameters from the DFT calculations as described in the literature.[27,65] Since all other contributions are small, they can be neglected as the Knight part dominates.

For all spectra the theoretical values of C_Q obtained from DFT calculations were used to simulate the spectra in the first place. In the cases of Sc, Yb and Lu the theoretical values did not match the experimental spectra well, here a better fit was
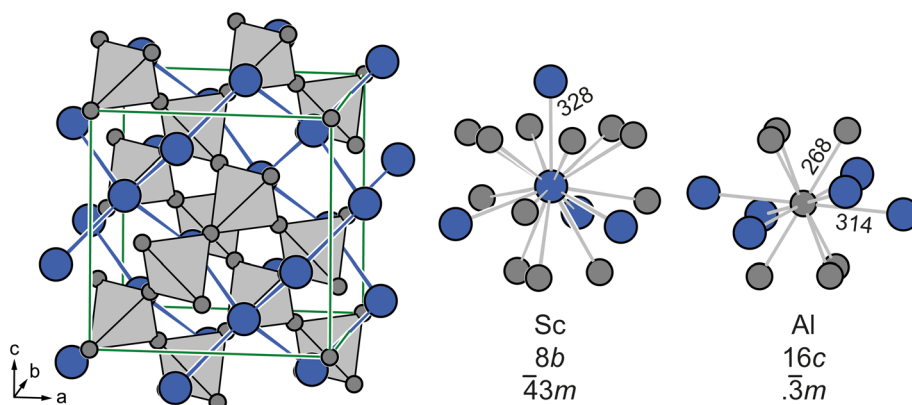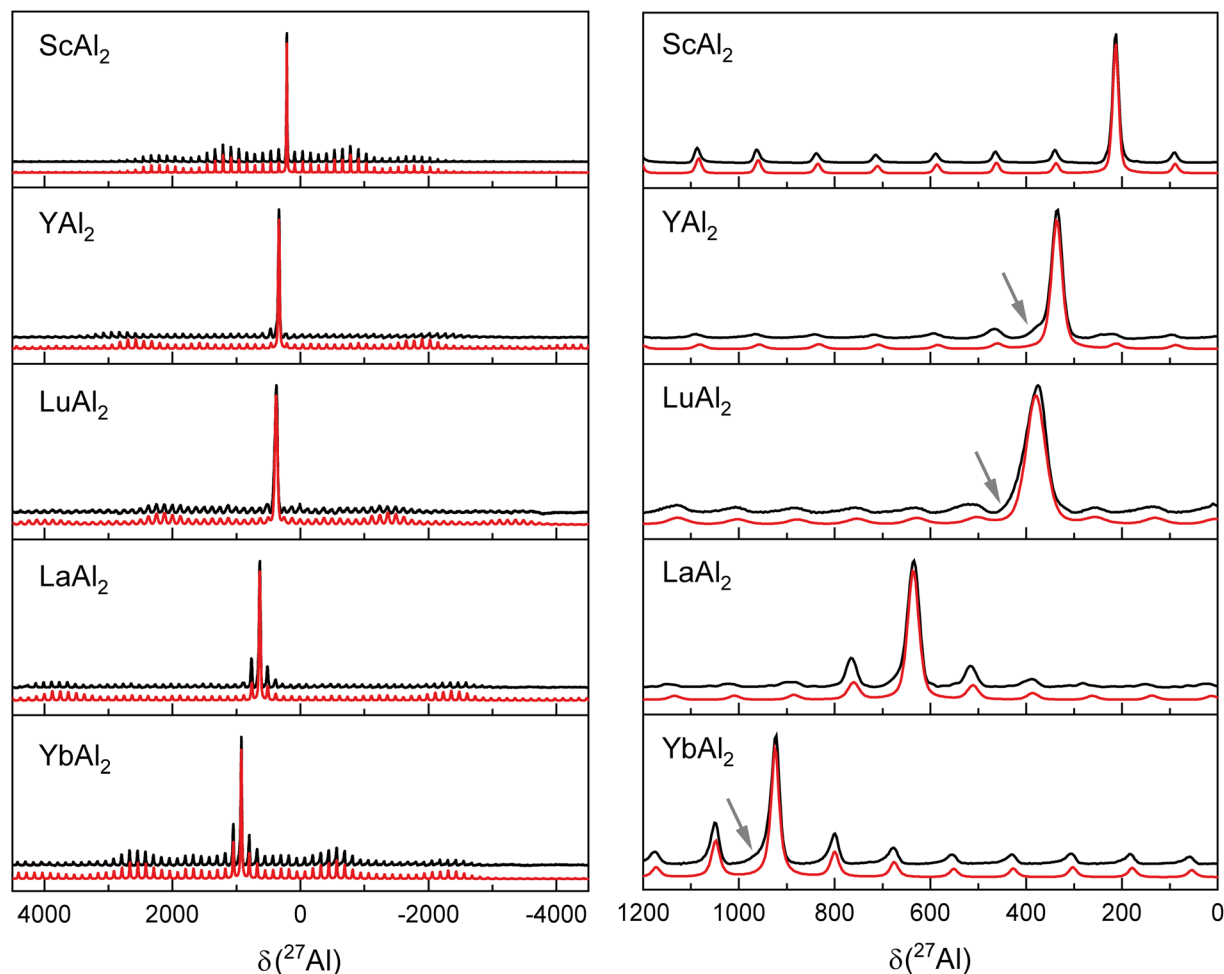

Fig. 3 (left) Unit cell of $ScAl_2$ ($MgCu_2$ type, $Fd\bar{3}m$) and coordination environments of the (middle) Sc (blue) and (right) Al (grey) atoms. Wyckoff positions and site symmetries as well as interatomic distances (in pm) are given.

Fig. 4 ^{27}Al solid state MAS NMR spectra (black) of the REAl$_2$ compounds (RE = Sc, Y, La, Yb, Lu) with simulations (red) of the central transition and the rotational sideband manifold (left). On the right site the central transition of each spectrum is shown. The asymmetric broadening is indicated by grey arrows.

Table 2 ^{27}Al and ^{45}Sc NMR parameters for the measured REAl$_2$ compounds (RE = Sc, Y, La, Yb and Lu). Isotropic shift δ (± 1 ppm), knight shift contribution δ_K, nuclear electric quadrupole coupling constants C_Q (± 0.05 MHz), electric field gradient asymmetry parameters η_Q (± 0.05), chemical shift anisotropy (dCS parameter) (± 5 ppm) and degrees of Gaussian (vs. Lorentzian) character of the central MAS signal

Compound		δ/ppm	δ_K/ppm	$C_{Q,theo}$/kHz	$C_{Q,exp}$/kHz	G/L	dCS/ppm	Lit.
ScAl$_2$	^{27}Al	213	213	884	1618	0.53	43	This work
	^{45}Sc	2279	2279	0	92	0	−22	This work
YAl$_2$	^{27}Al	336	343	3466		0.49	−17	This work
	^{27}Al	364					30	38
LaAl$_2$	^{27}Al	636	648	4626		0.53	−108	This work
	^{27}Al	600			4630/5139		0	38–40
YbAl$_2$	^{27}Al	924	926	2072	2488	0.21	−188	This work
	^{27}Al	1100			2300/2580			39 and 41
LuAl$_2$	^{27}Al	379	381	2034	2794	0.65	−14	This work
	^{27}Al	386			2840		48/32	38

found using the DMFit simulation program.[46] Fig. 5 (left) exemplarily shows the ^{27}Al MAS spectrum for YbAl$_2$, where the intensity profile simulated based on the DFT-calculated C_Q does not match to the recorded spectrum, while Fig. 5 (right) shows the results from the fit. For quadrupolar coupling constants >3 MHz it is more difficult up to impossible to deter-

mine the C_Q parameter via the analysis of the experimental sideband spinning pattern because it extends over a too large spectral region which exceeds the available spectral bandwidth.[33] At the same time, it also becomes clear that a determination of C_Q from the line shape of the central transition is not possible because it is featureless and can be described well
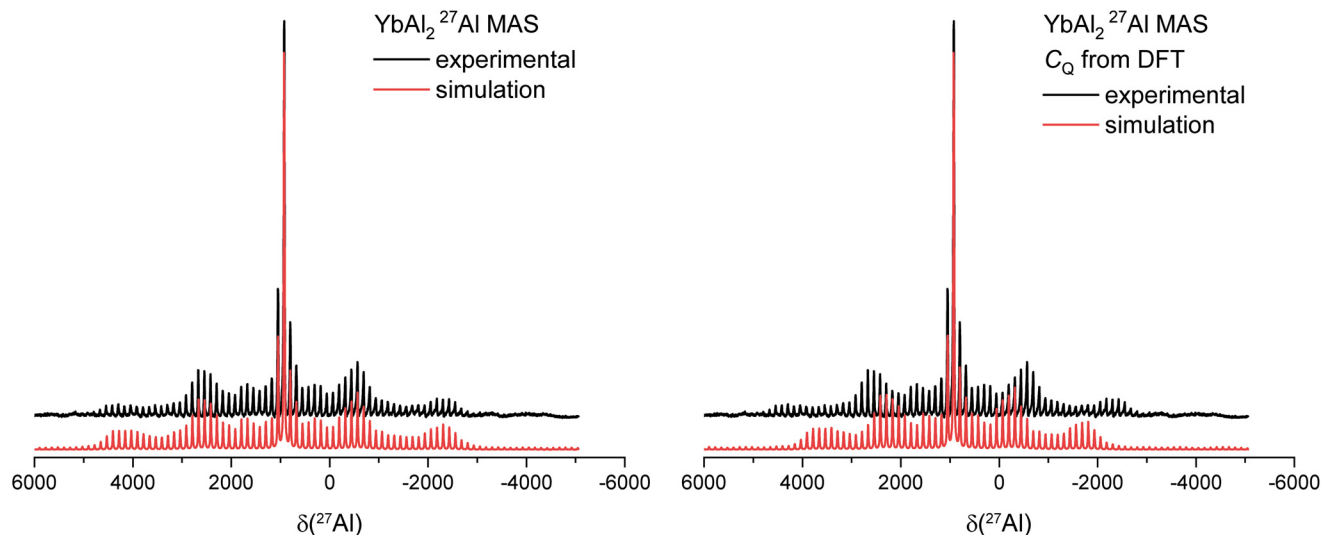
Fig. 5 ^{27}Al MAS spectrum of YbAl$_2$ fitted with an experimental determined value of C_Q (left) *versus* the C_Q value obtained by DFT calculations (right).

with a Gaussian-Lorentz simulation (Fig. 5). This is also the case for the La and Y compounds. Here, the quadrupolar coupling parameters obtained *via* DFT calculations were used and no refinement was performed. Finally, one can observe that the spinning sideband pattern intensities are asymmetric to the central transition. This indicates that chemical shift anisotropy (CSA) is present.

It should be noted that the samples of YAl$_2$, YbAl$_2$ and LuAl$_2$ show a shoulder to the left side of the central transition. Similar asymmetric line broadening of the central transition of the YAl$_2$ and LuAl$_2$ spectra is also observed in the literature.[38] That observation is consistent with the fact that significant strain is observed in the PXRD patterns for all compounds (*vide supra*). To overcome the influence of strain within the structure, the arc-melted sample of LuAl$_2$ was exemplarily heat treated and reinvestigated by NMR. It should be mentioned that the influence of annealing was already investigated in the literature.[38] Fig. 6 shows a comparison of the ^{27}Al MAS spectra of as-cast LuAl$_2$ and after annealing. It can be observed that the anisotropically broadened central transition is still present, but the line width of the transition gets smaller (by a factor of 2) after the thermal treatment. This observation is in line with the reduction in strain in the PXRD pattern.

The ^{27}Al and ^{45}Sc spectra of ScAl$_2$ are shown in Fig. 7. For the ^{45}Sc MAS NMR also one sharp central line, originating from the $|+1/2\rangle \leftrightarrow |-1/2\rangle$ transition is observed, a potential spinning side band manifold is caused by the $|\pm1/2\rangle \leftrightarrow |\pm3/2\rangle$, $|\pm3/2\rangle \leftrightarrow |\pm5/2\rangle$ and $|\pm5/2\rangle \leftrightarrow |\pm7/2\rangle$ transitions, which are observable due to quadrupolar interactions.[66] The DFT calculations on ScAl$_2$ suggest a C_Q and η_Q of zero, but simulations of the observed spinning sideband manifold give a rather small value of C_Q = 92 kHz. A possible explanation for the difference between experiment and theory in this case could be that the DFT calculations are performed with a non-defective, perfect structure, which is not true for as synthesized compounds.
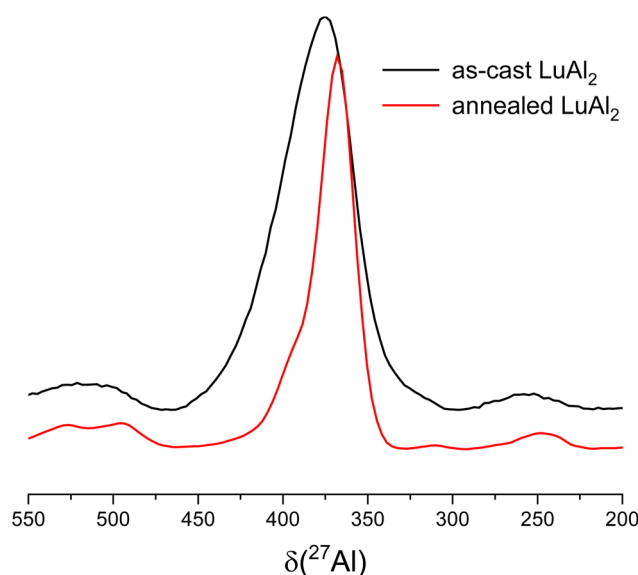

Fig. 6 Comparison of the central transition in the ^{27}Al MAS spectra of as-cast (black) and annealed (red) LuAl$_2$.

Here disorder and strain can play a significant role. And even if ScAl$_2$ exhibits a rather small strain as refined from the powder X-ray diffraction data, NMR as a local probe can visualize even these small influences. This observation can also explain, why the calculated C_Q parameters in most cases are smaller than the experimental values (Table 2). The same is true for the ^{27}Al MAS spectrum for ScAl$_2$, here the experimental C_Q value is double the size of the theoretical one (Table 2), similar to what has been observed for YbAl$_2$ (*vide supra*).

Of these five compounds, YAl$_2$, LaAl$_2$, YbAl$_2$ and LuAl$_2$ have already been investigated by ^{27}Al NMR investigations.[38–41] For these, a full characterization, along with partial quantum chemical investigations has been conducted and the results
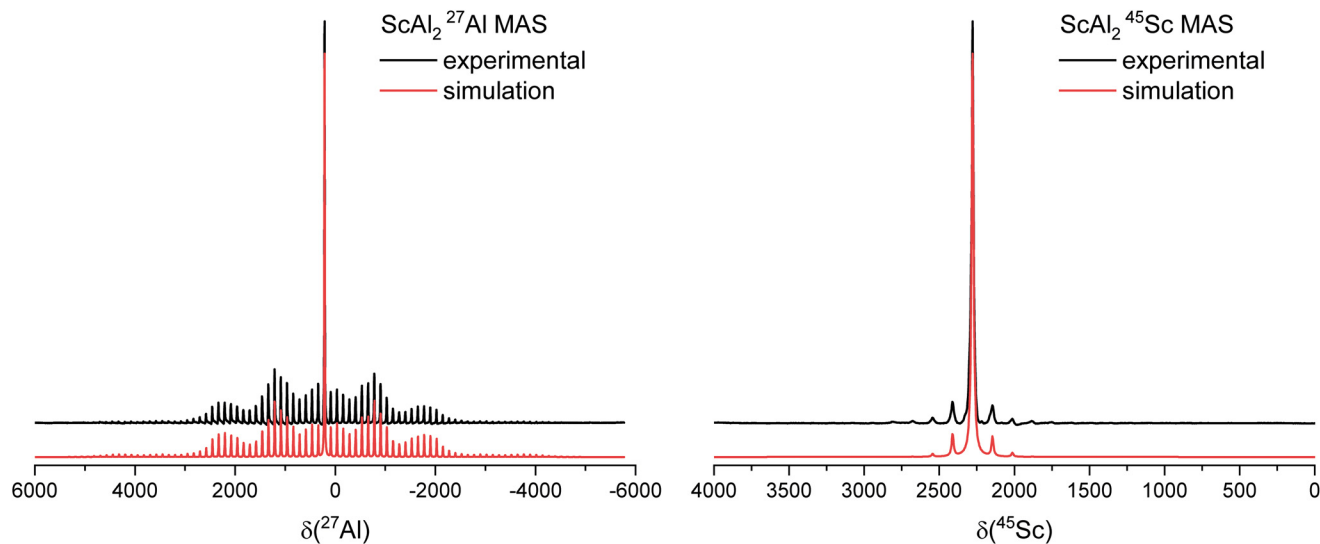
Fig. 7 ^{27}Al (left) and ^{45}Sc (right) MAS spectrum of ScAl$_2$ (black) along with the fitted spectra (red).

from the literature have been compiled in Table 2 along with the results of this study. The resonance shifts of the central transitions are in good (YAl$_2$ and LuAl$_2$) to fair (LaAl$_2$) agreement with the ones reported by Yuan *et al.*,[38] while the quadrupolar coupling constants C_Q are a good match. For YbAl$_2$, only the quadrupolar coupling constants C_Q had been reported before by Jaccarino[39] and Barnes,[41] which is in good agreement with the results reported here. In contrast, for ScAl$_2$, no

investigations regarding the resonance shift and the quadrupolar coupling have been reported. Here, only the Knight shift contribution and an estimate of the s-electron densities have been reported.[67]

3.4 Raman spectroscopy

Raman spectroscopic measurements of the title compounds have been conducted using crystallites of the polycrystalline
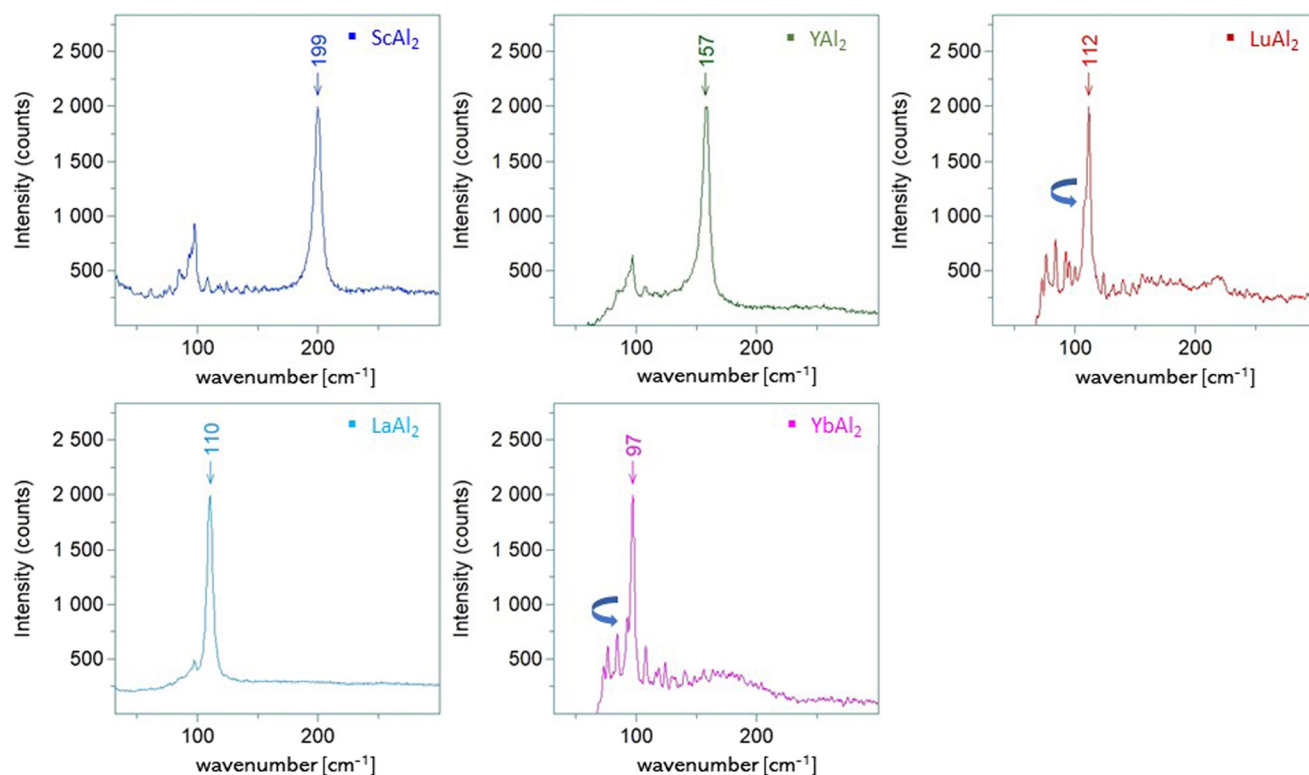

**Fig. 8** Raman spectra of REAl$_2$ (RE = Sc, Y, Lu, La, Yb), the arrows mark the shoulders at RE = Lu, Yb.

Table 3 Raman bands of REAl$_2$ compounds, measurements conducted in this study are the average of 6 measurements, respectively, at room temperature

RE	Position T$_{2g}$/cm^{-1}	FWHM/cm^{-1}	Reference	Position T$_{2g}$/cm^{-1}	FWHM/cm^{-1}	Ref.
Sc	198–199	6.3	This work			
Y	157–160	5.4	This work			
Gd				118	4	68
Dy				117	5	68
Sm				115		69
Lu	111–112	3.4	This work			
	108 (shoulder)	3.8	This work			
La	110–112	4.9	This work	112	5	68
Ce				109	7	68
Yb	96–97	2.7	This work	95	10	68
Eu				96	4	68

FWHM: Full width at half maximum.

sample under a Raman microscope 532 nm and 633 nm laser excitation. All five compounds show one band in the measured range of 10 to 900 cm^{-1} (Fig. 8) originating from the respective intermetallic compound. The bands around 100 cm^{-1} could be assigned to water. According to the investigations of Güntherodt et al.,[68] the Γ_{25}' (T_{2g}) Raman-active mode in the cubic Laves-phase is caused by the rare-earth atoms (8b site) with their diamond-type arrangement. They investigated different REAl$_2$ compounds (RE = La, Ce, Eu, Gd, Dy, Yb) and observed modes with peak maxima ranging from 95 for YbAl$_2$ to 118 cm^{-1} for GdAl$_2$ (Table 3). Their data could be confirmed for the cases of LaAl$_2$, YbAl$_2$ and LuAl$_2$ and furthermore extended by the measurements of ScAl$_2$ and YAl$_2$ with maxima at 199 and 157–160 cm^{-1} and half-width values of 6 and 5 cm^{-1}, respectively. The positions for LaAl$_2$ and YbAl$_2$ as well as half-widths for LuAl$_2$ agree with the ones in the literature.[68] A striking feature, however, is that EuAl$_2$ and YbAl$_2$ exhibit by far the lowest wavenumbers. This nicely correlates with their formal oxidation state being divalent (EuAl$_2$) and intermediate valent (YbAl$_2$). The amplitudes of the YbAl$_2$ oscillation are weak; the cause could be the superposition with water vibrations as well as the intermediate valence state. YbAl$_2$ shows an asymmetric broadening of the band in direction to smaller wavenumbers and Güntherodt et al., observed a half width of 10 cm^{-1}.[68] Analogously, a shoulder at 108 cm^{-1} was detected for LuAl$_2$ next to the main band at 112 cm^{-1}. Since here no intermediate valence behaviour is possible, this feature might be caused by the significant strain in the material.

Like with the NMR resonances, the Raman bands observed for the different REAl$_2$ members show significant differences. When the Raman bands are plotted versus the unit cell parameter a (Fig. 9), two trends are observed. For the members of group 3, the Raman bands shift almost linearly within the group from Sc (200 cm^{-1}) to Y (158 cm^{-1}) to La (110 cm^{-1}). In contrast, within the lanthanide series there are only small variations, with the exceptions of EuAl$_2$ and YbAl$_2$. The latter, however, exhibit divalent Eu^{2+} or intermediate valent Yb$^{2.4+}$ cations, hence, the unusually large lattice parameters and low
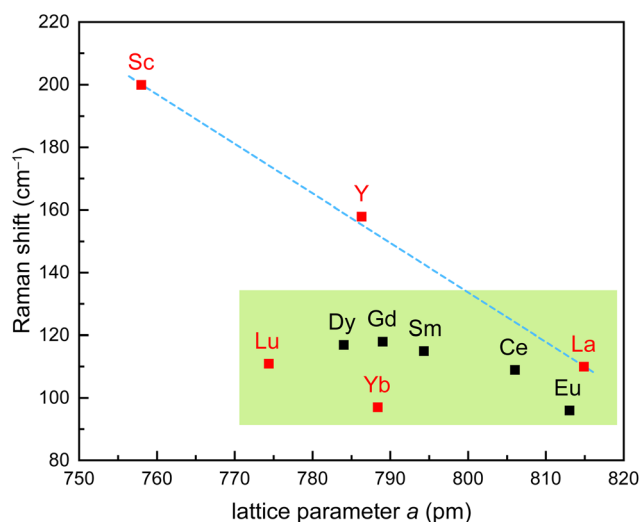
Fig. 9 Raman shifts plotted versus the lattice parameters of the REAl$_2$ compounds. The almost linear trend within group 3 is highlighted by the blue dashed line. The lanthanide compounds are highlighted by the green box.

Raman shifts. The differences could be explained by the electron configurations. While Sc, Y and La are rather transition metals, the other elements are f-elements and exhibit electron configurations of [Xe] 4f^n with $n \geq 1$.

3.5 Quantum chemistry

The electronic structures of the title compounds were analysed using density functional theory (DFT) calculations. The electron density of states (DOS) curves of REAl$_2$ (RE = Sc, Y, La, Yb, Lu) and the partial s-electron DOS (p-DOS) of the Al atoms in each compound are plotted in Fig. 10. There is a substantial density of states at the Fermi level for all five compounds, indicating metallic behaviour, in line with the silvery shiny metallic appearance. The calculated Bader effective charges for REAl$_2$ (RE = Sc, Y, La, Yb, Lu) are listed in Table 4. In all five compounds, the RE atoms have positive, while the Al atoms have negative charges, rendering them aluminides. The
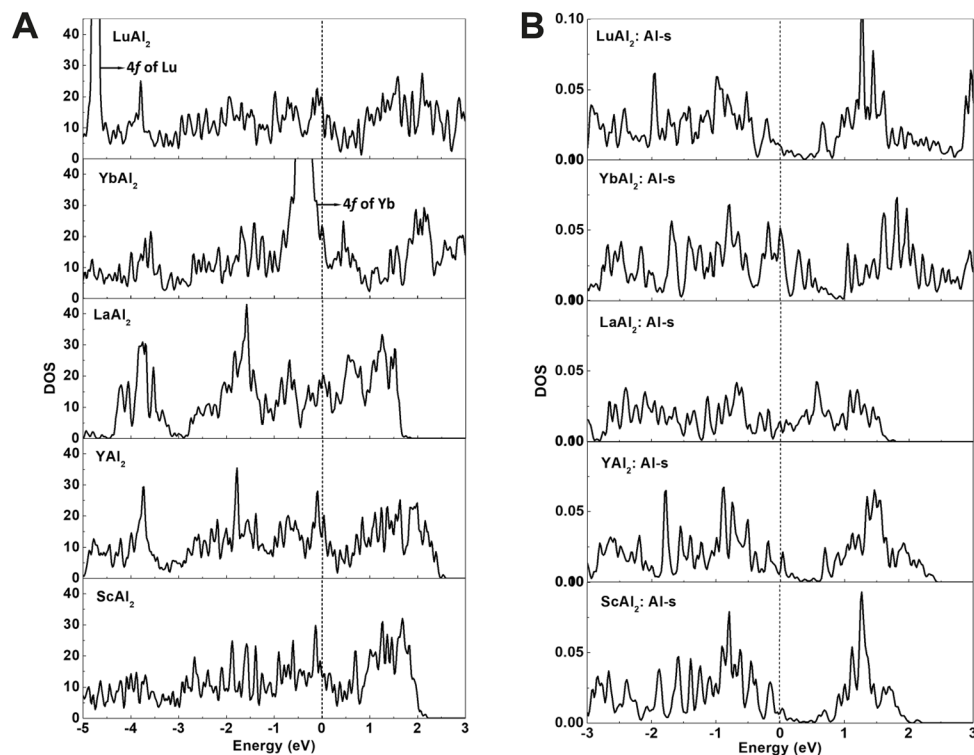
Fig. 10 (A) Total density of states and (B) Al s-electron partial density of states (per Al atom) of REAl$_2$ (RE = Sc, Y, La, Yb, Lu) from non-spin-polarized DFT calculations, dotted line indicates Fermi level.

Table 4 Bader charges and s-electron densities (DOS per Al atom, states/eV) of the Al atoms at the Fermi level in the REAl$_2$ series (RE = Sc, Y, La, Yb, Lu) obtained from non-spin-polarized DFT calculations

REAl$_2$	ScAl$_2$	YAl$_2$	LaAl$_2$	YbAl$_2$	LuAl$_2$
Charge on RE	+1.23	+1.25	+0.97	+1.08	+1.14
Charge on Al	−0.61	−0.62	−0.48	−0.54	−0.57
DOS per Al atom	0.00670	0.00851	0.0144	0.0511	0.0102

effective charges on the RE atoms are significantly smaller than +3 indicating weak ionic bonding between the RE$^{\delta+}$ cations and the [Al$_2$]$^{\delta-}$ polyanionic network. When looking at the trend of the Pauling electronegativities (EN)[18] (Sc: χ = 1.36; Y: χ = 1.22; La: χ = 1.1; Yb: χ = 1.1; Lu: χ = 1.27) one would expect larger positive effective charges of La and Yb, compared to Sc, Y and Lu, contrary to the Bader charges (Table 4). To
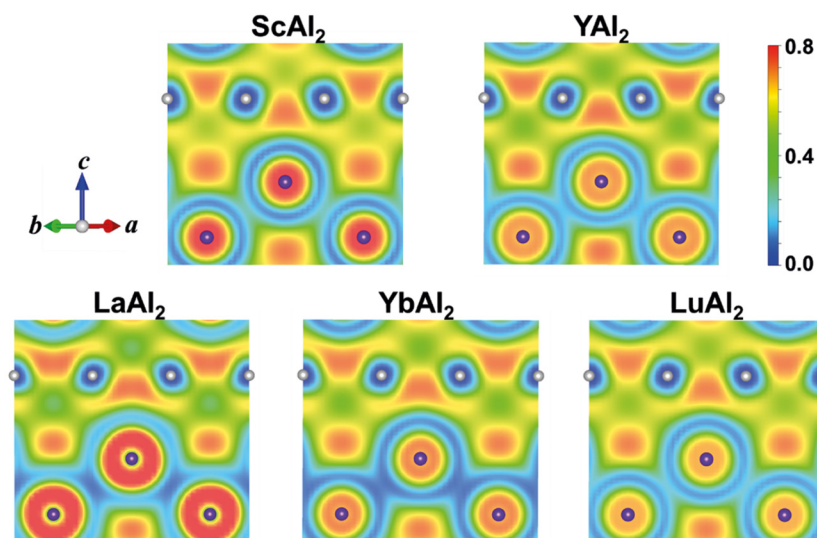
Fig. 11 Electron localization function (ELF) plots of the (110) plane for REAl$_2$ (RE = Sc, Y, La, Yb, Lu). Purple and grey spheres represent RE and Al atoms, respectively.
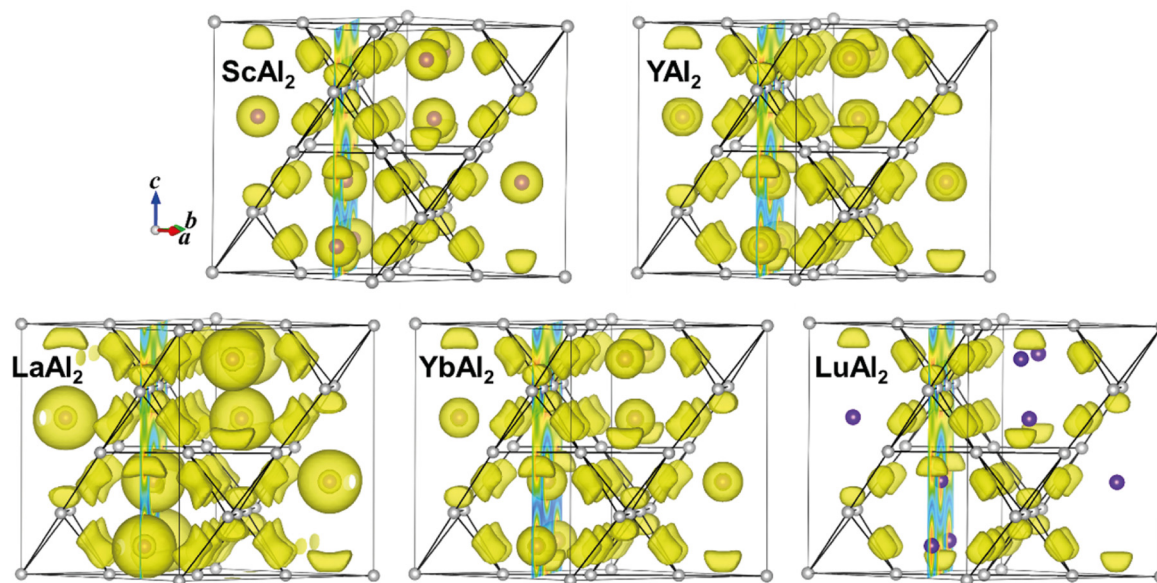
Fig. 12 Electron localization functions (ELF) plots for REAl$_2$ (RE = Sc, Y, La, Yb, Lu) at iso-surface level of 0.70. Purple and grey spheres represent RE and Al atoms, respectively.

better understand the chemical bonding in REAl$_2$, electron localization functions have been examined and the results are shown in Fig. 11 and 12. Fig. 11 shows a high electron localization between nearest neighbour Al atoms, signalling covalent Al–Al interactions, which form the [Al$_2$]$^{\delta-}$ network. This is also supported by the iso-surface plotted in Fig. 12. It is worth noting that the electron localization is not evenly distributed around the Al–Al bond but prefers the side of bond facing the RE atom, which may be caused by the orbital overlap between Al and the RE atoms indicating partial multi-centre bonding. There is a high electron localization between La (or Yb) and the Al atoms in LaAl$_2$ (or YbAl$_2$), indicating stronger La–Al (Yb–Al) covalent interactions (weaker ionic interactions respectively) compared to those in ScAl$_2$, YAl$_2$ and LuAl$_2$, providing an explanation for the small effective positive charges on La (or Yb), however, being in contrast with the EN. It is possible that the 5d orbitals in LaAl$_2$ can overlap more with Al s/p orbitals, resulting in stronger covalent La–Al interactions, or, as suggest before, multi-centre bonding takes place. For YbAl$_2$, based on the DOS in Fig. 10, the 4f orbital is right below the Fermi level, which might contribute to the Yb–Al orbital overlap and leading to strong Yb–Al covalent interactions. In addition, Yb is a so-called two-electron metal, despite Sc, Y, La and Lu being three-electron metals. Therefore, a reduced Bader charge on the Yb atoms is expected from this point of view. However, YbAl$_2$ is an intermediate valent compound[60,61] and exhibits partial Yb^{3+} character, making the bonding situation even more complicated.

Fig. 13 finally shows the correlation between the s-electron DOS of the Al atoms at the Fermi level plotted *versus* the calculated Knight shift contribution δ_K. As for the Raman measurements, also a correlation between the two and three electron metals can be observed. In YbAl$_2$, a significantly, almost by a
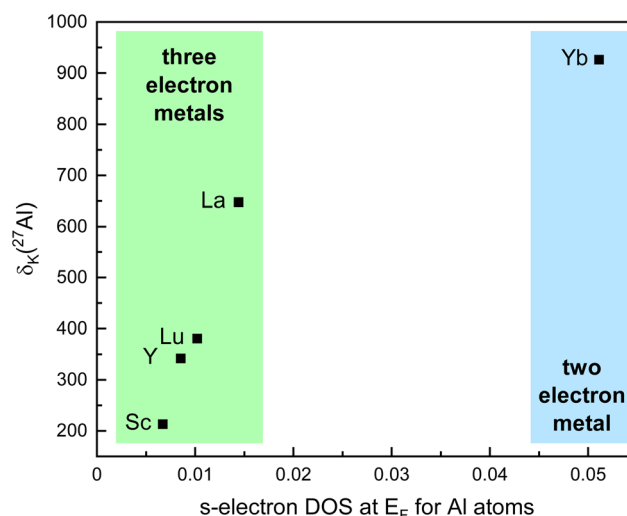

Fig. 13 Al atom s-electron pDOS at E_F plotted *versus* δ_K. The green and blue boxes indicate the formally two and three electron metals.

factor of 10, larger s-electron DOS at E_F is observed leading to a dramatic shift in the ^{27}Al NMR signal. Within the close-shell compounds, an almost linear increase of the Knight shift δ_K *versus* the s-electron DOS is visible.

4 Conclusion

The close-shell rare-earth aluminides REAl$_2$ with RE = Sc, Y, La and Lu as well as intermediate valent YbAl$_2$ (all cubic MgCu$_2$ type) were synthesized from the elements and structu-

rally characterized by powder X-ray diffraction. All compounds are X-ray pure; however, significant strain could be observed for the Y, Yb and Lu compounds. Annealing of LuAl$_2$ decreased the strain. ^{27}Al solid-state MAS NMR spectra were recorded for all compounds and in addition, ^{45}Sc solid-state MAS NMR spectroscopic investigations for ScAl$_2$ were conducted. All ^{27}Al spectra exhibit a single central transition, in line with one crystallographic Al site, the same is true for the ^{45}Sc spectrum. However, in agreement with the PXRD investigations, the main transitions of YAl$_2$, YbAl$_2$ and LuAl$_2$ show an asymmetry which is probably caused by the strain of the material. Comparing investigations of annealed LuAl$_2$ show a significantly sharper signal. The spectra were fitted using NMR parameters obtained from quantum-chemical calculations, however, not for all compounds the calculated values are in line with the experimentally observed ones, again caused by the internal strain. Raman spectra collected of all title compounds also show the strain inherent to the material. A comparison of the Raman shifts with respect to the structural data shows that the shift in the Raman signals can be explained by the variations in the interatomic distances and the electronic situation of the respective RE element. Finally, the bonding situation within the REAl$_2$ members was assessed using Bader charge calculations and electron localization function (ELF). Bader charges clearly indicate the formation of aluminides due to the negatively charged $[Al_2]^{\delta-}$ framework, in line with the Pauling electronegativities. The peculiarities in the Bader charges can be attributed to the oxidation state of the RE atoms and a multicentre bond formation. A comparison of the s-electron density at E_F with the Knight shift contribution to the ^{27}Al NMR resonance shows a linear dependency for the close-shell atoms, Yb, however, differs, due to the intermediate valence state.

Author contributions

All authors have accepted responsibility for the entire content of this submitted manuscript and approved the submission.

Conflicts of interest

The authors declare no conflicts of interest regarding this article.

Acknowledgements

References

1 O. Janka, Metallic light-weight alloys: Al, Ti, Mg, in *Applied Inorganic Chemistry*, ed. R. Pöttgen, T. Jüstel and C. Strassert, De Gruyter, 2022, pp. 158–173.

2 F. Ostermann, *Anwendungstechnologie Aluminium*, Springer Vieweg, Berlin, Heidelberg, 2014.

3 R. Kilaas, V. Radmilovic and U. Dahmen, *Mater. Res. Soc. Symp. Proc.*, 2001, **589**, 273–278.

4 B. Heying, R.-D. Hoffmann and R. Pöttgen, *Z. Naturforsch.*, 2005, **60b**, 491–494.

5 S. J. Andersen, C. D. Marioara, J. Friis, S. Wenner and R. Holmestad, *Adv. Phys.: X*, 2018, **3**, 1479984.

6 P. Villars and K. Cenzual, *Pearson's Crystal Data: Crystal Structure Database for Inorganic Compounds*, ASM International®, Materials Park, Ohio, USA, 2023.

7 H. Nowotny, E. Wormnes and A. Mohrnheim, *Z. Metallkd.*, 1940, **32**, 39–42.

8 R. E. Rundle and A. S. Wilson, *Acta Crystallogr.*, 1949, **2**, 148–150.

9 O. J. C. Runnalls, *JOM*, 1953, **5**, 1460–1462.

10 O. J. C. Runnalls, *Can. J. Chem.*, 1956, **34**, 133–145.

11 A. Iandelli, *Natl. Phys. Lab. (U. K.), Symp.*, 1951, 3F2–3F11.

12 V. B. Compton and B. T. Matthias, *Acta Crystallogr.*, 1959, **12**, 651–654.

13 J. H. Wernick and S. Geller, *Trans. Metall. Soc. AIME*, 1960, **218**, 866–868.

14 F. Stein and A. Leineweber, *J. Mater. Sci.*, 2021, **56**, 5321–5427.

15 E. Bauer, E. Gratz and G. Adam, *J. Phys. F: Met. Phys.*, 1986, **16**, 493.

16 A. T. Burkov, M. Vedernikov and E. Gratz, *Physica B Condens. Matter*, 1992, **176**, 263–274.

17 A. K. Pathak, D. Paudyal, K. A. Gschneidner and V. K. Pecharsky, *J. Appl. Phys.*, 2014, **115**, 17E109.

18 J. Emsley, *The Elements*, Clarendon Press, Oxford University Press, Oxford, New York, 1998.

19 J. Donohue, *The Structures of the Elements*, Wiley, New York, 1974.

20 R. K. Harris, E. D. Becker, S. M. Cabral de Menezes, P. Granger, R. E. Hoffman and K. W. Zilm, *Pure Appl. Chem.*, 2008, **80**, 59–84.

21 N. J. Stone, *At. Data Nucl. Data Tables*, 2016, **112**, 1–28.

22 A. Putnis, *Phys. Chem. Miner.*, 1996, **23**, 247–247.

23 M. Haouas, F. Taulelle and C. Martineau, *Prog. Nucl. Magn. Reson. Spectrosc.*, 2016, **95**, 11–36.

24 A. T. Bell, *Colloids Surf., A*, 1999, **158A**, 221–234.

25 G. Engelhardt, Characterization of Zeolite Catalysts and Related Materials by Multinuclear Solid-State NMR Spectroscopy, In *Surface Science: Principles and Current Applications*, ed. R. J. MacDonald, E. C. Taglauer and

K. R. Wandelt, Springer Berlin Heidelberg, Berlin, Heidelberg, 1996, pp. 321–330.

26 A. L. Blumenfeld and J. J. Fripiat, *Magn. Reson. Chem.*, 1999, **37**, S118–S125.

27 C. Benndorf, H. Eckert and O. Janka, *Acc. Chem. Res.*, 2017, **50**, 1459–1467.

28 M. Radziewowski, C. Benndorf, S. Haverkamp, H. Eckert and O. Janka, *Z. Naturforsch.*, 2016, **71b**, 553–566.

29 C. Benndorf, O. Niehaus, H. Eckert and O. Janka, *Z. Anorg. Allg. Chem.*, 2015, 168–175.

30 F. Stegemann, C. Benndorf, Y. Zhang, M. Bartsch, H. Zacharias, B. P. T. Fokwa, H. Eckert and O. Janka, *Inorg. Chem.*, 2017, **56**, 1919–1931.

31 C. Benndorf, F. Stegemann, S. Seidel, L. Schubert, M. Bartsch, H. Zacharias, B. Mausolf, F. Haarmann, H. Eckert, R. Pöttgen and O. Janka, *Chem. – Eur. J.*, 2017, **23**, 4187–4196.

32 F. Stegemann, C. Benndorf, Y. Zhang, M. Bartsch, H. Zacharias, B. P. T. Fokwa, H. Eckert and O. Janka, *Z. Anorg. Allg. Chem.*, 2017, **643**, 1379–1390.

33 F. Stegemann, C. Benndorf, T. Bartsch, R. S. Touzani, M. Bartsch, H. Zacharias, B. P. T. Fokwa, H. Eckert and O. Janka, *Inorg. Chem.*, 2015, **54**, 10785–10793.

34 F. Stegemann, T. Block, S. Klenner, Y. Zhang, B. P. T. Fokwa, C. Doerenkamp, H. Eckert and O. Janka, *Eur. J. Inorg. Chem.*, 2021, **2021**, 3832–3845.

35 F. Stegemann, T. Block, S. Klenner, Y. Zhang, B. P. T. Fokwa, A. Timmer, H. Mönig, C. Doerenkamp, H. Eckert and O. Janka, *Chem. – Eur. J.*, 2019, **25**, 10735–10747.

36 M. Radziewowski, F. Stegemann, C. Doerenkamp, S. F. Matar, H. Eckert, C. Dosche, G. Wittstock and O. Janka, *Inorg. Chem.*, 2019, **58**, 7010–7025.

37 C. Benndorf, H. Eckert and O. Janka, *Dalton Trans.*, 2017, **46**, 1083–1092.

38 C. C. Yuan, Y. F. Yang, X. K. Xi, J. Cui and J. F. Xiang, *Solid State Nucl. Magn. Reson.*, 2012, **41**, 28–31.

39 V. Jaccarino, B. T. Matthias, M. Peter, H. Suhl and J. H. Wernick, *Phys. Rev. Lett.*, 1960, **5**, 251–253.

40 K. Betsuyaku and H. Harima, *J. Magn. Magn. Mater.*, 2001, **226–230**, 199–201.

41 R. G. Barnes, W. H. Jones and T. P. Graham, *Phys. Rev. Lett.*, 1961, **6**, 221–223.

42 R. Pöttgen, T. Gulden and A. Simon, *GIT Labor-Fachz.*, 1999, **43**, 133–136.

43 R. Pöttgen, A. Lang, R.-D. Hoffmann, B. Künnen, G. Kotzyba, R. Müllmann, B. D. Mosel and C. Rosenhahn, *Z. Kristallogr.*, 1999, **214**, 143–150.

44 Bruker AXS Inc., *Topas, Version 5*, Karlsruhe, Germany, 2014.

45 Bruker Corp., *Topspin, Version 2.1*, Karlsruhe, 2008.

46 D. Massiot, F. Fayon, M. Capron, I. King, S. Le Calvé, B. Alonso, J.-O. Durand, B. Bujoli, Z. Gan and G. Hoatson, *Magn. Reson. Chem.*, 2002, **40**, 70–76.

47 P. E. Blöchl, *Phys. Rev. B*, 1994, **50**, 17953–17979.

48 G. Kresse and D. Joubert, *Phys. Rev. B*, 1999, **59**, 1758–1775.

49 G. Kresse and J. Furthmüller, *Phys. Rev. B*, 1996, **54**, 11169–11186.

50 G. Kresse and J. Furthmüller, *Comput. Mater. Sci.*, 1996, **6**, 15–50.

51 J. P. Perdew, K. Burke and M. Ernzerhof, *Phys. Rev. Lett.*, 1996, **77**, 3865–3868.

52 E. Sanville, S. D. Kenny, R. Smith and G. Henkelman, *J. Comput. Chem.*, 2007, **28**, 899–908.

53 G. Henkelman, A. Arnaldsson and H. Jónsson, *Comput. Mater. Sci.*, 2006, **36**, 354–360.

54 W. Tang, E. Sanville and G. Henkelman, *J. Phys.: Condens. Matter*, 2009, **21**, 084204.

55 A. Savin, R. Nesper, S. Wengert and T. F. Fässler, *Angew. Chem.*, 1997, **109**, 1892–1918.

56 B. Silvi and A. Savin, *Nature*, 1994, **371**, 683–686.

57 R. D. Shannon, *Acta Crystallogr.*, 1976, **A32**, 751.

58 R. D. Shannon and C. T. Prewitt, *Acta Crystallogr.*, 1969, **B25**, 925.

59 A. Gleissner, W. Potzel, J. Moser and G. M. Kalvius, *Phys. Rev. Lett.*, 1993, **70**, 2032–2035.

60 A. Iandelli and A. Palenzona, *J. Less-Common Met.*, 1972, **29**, 293–297.

61 E. E. Havinga, K. H. J. Buschow and H. J. van Daal, *Solid State Commun.*, 1973, **13**, 621–627.

62 V. N. Rechkin, L. K. Lamikhov and T. I. Samsonova, *Sov. Phys. Crystallogr.*, 1964, **9**, 325–327.

63 H. N. Nowotny, *Z. Metallkd.*, 1942, **34**, 22–24.

64 S. E. Haszko, *Trans. Metall. Soc. AIME*, 1960, **218**, 958.

65 S. Engel, E. C. J. Gießelmann, L. E. Schank, G. Heymann, K. Brix, R. Kautenburger, H. P. Beck and O. Janka, *Inorg. Chem.*, 2023, DOI: **10.1021/acs.inorgchem.2c04391**.

66 H. Eckert and R. Pöttgen, *Z. Anorg. Allg. Chem.*, 2010, **636**, 2232–2243.

67 E. P. Chock, R. A. B. Devine, S. A. Dodds, R. Orbach and L. Tippie, *J. Phys. F: Met. Phys.*, 1977, **7**, 1097–1102.

68 G. Güntherodt, A. Jayaraman, G. Batlogg, M. Croft and E. Melczer, *Phys. Rev. Lett.*, 1983, **51**, 2330–2332.

69 J. Su and C. Zhu, *Mater. Res. Bull.*, 2003, **38**, 2025–2029.